Chapter 2

Experimental Methodology

2.1 Introduction

The following section contains complete descriptions of the materials, equipment, and methodology employed in all research pertaining to this thesis. X-ray diffraction experiments have been carried out using a facility that utilizes a 4-port rotating anode x-ray generator. The two wide-angle diffraction ports have permanently mounted diffractometers and detectors which have been optimized for the acquisition of polymer x-ray spectra. Each port has its own computer equipment to communicate with the data acquisition and stepping motor electronics allowing for partial automation of polymer spectra acquisition (see Fig. 2.6).

P3AT samples studied as part of this thesis were received from three different sources. The primary polymer samples were synthesized by the Heeger group at the University of California at Santa Barbara. Other samples were synthesized by Neste Oy, and samples with the highest regiospecificity were synthesized by the McCullough group at Carnegie Mellon University. The specific synthesis and preparation methods will be discussed later in the chapter.

Necessary data refinement and analysis was preformed on various Digital VMS/VAX workstations. All refinement and analysis software was written and developed within the Winokur group here at the University of Wisconsin-Madison.

2.2 X-Ray Diffraction Facility

2.2.1 X-Ray Generator

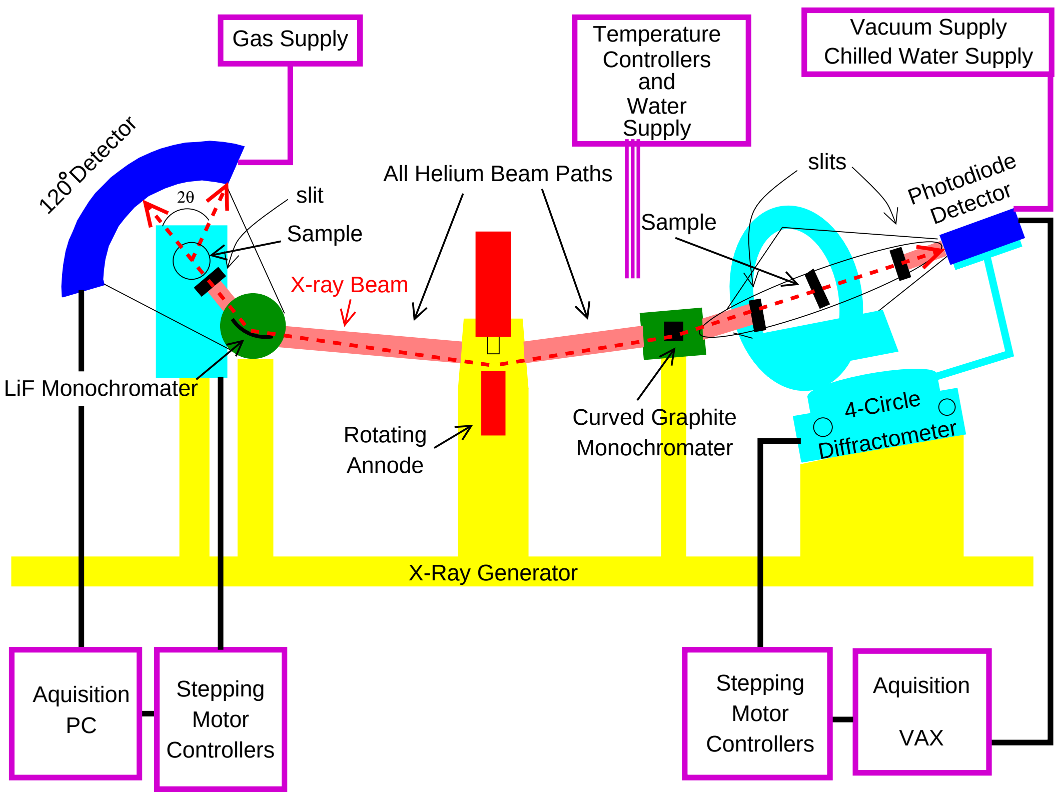

Figure 2.6: Schematic description of the x-ray diffraction facility used in this work.

The primary x-ray source utilized in this work has been a 15-KW Elliot GX-21 rotating anode generator (*circa* 1980) with a copper target ($\lambda_{K_\alpha} = 1.542$Å) and two wide angle diffraction ports. One diffraction port consists of a 4-circle

Huber diffractometer with a curved graphite monochromating crystal and silicon photodiode array detector, while the other port consists of a 120° "wire" detector with a LiF monochrometer (see Fig. 2.6). The generator was operated at powers ranging between 8KW and 11KW with a normal operation of 8KW consisting of a filament current of 200ma and a target-filament potential difference of 40KV. The generator was never operated at the designed maximum power of 15KW. The homemade filaments consisted of .0142" diameter, 1% thoriated tungsten wire wrapped around a .05" rod so that finished filaments consisted of approximately 30 coils over a 15mm length. Properly installed filaments had lifetimes of around 3 months while improperly installed versions lasted around 3-4 weeks at 8KW. The generator provided approximately constant x-ray flux over the lifetime of a filament with losses originating mainly from tungsten buildup on the anode target. This buildup was periodically removed by polishing the copper anode, minimizing flux loss due to this effect.

2.2.2 4-Circle Diffractometer

This x-ray diffraction port is optimized for the acquisition of both the equatorial and non-equatorial scattering from polymer films. It has a vertically bent HOPG graphite crystal used as both a monochrometer and beam collimator. The cross-sectional area of the incident x-ray beam at the sample was adjusted to $\sim 3.0 \times 2.0$ mm^2 (height $\times$ width). Helium beam paths insured a minimum amount of air scattering without resorting to completely evacuated beam paths. Samples were placed in a 4-circle Huber diffractometer which was a combination of a 2-circle Eulerian cradle (Model 511.1) and a 2-circle goniometer (Model 424). The rotational motions of the diffractometer were driven by four standard stepping motors, two for the χ- and ϕ-circles on the Eulerian cradle, and two for the

2θ- and ω-circles on the goniometer (complete descriptions of stepping motor functions are included in 2.4.2).

A position sensitive array detector consisting of a refrigerated silicon diode array (EG&G Princeton Applied Research M1412XR) and associated interface electronics (EG&G M1461 Optical Multichannel Analyzer) was located ~30 cm from the scattering center and subtended a 2θ arc of ~4.5°. The detector's spatial resolution was set by forming various pixel groups from the detector's 960 accessible $25\mu m$ x 2.5 mm pixels. Typical counting rates, for a single group of 16 pixels at the most intense reflection of $40\mu m$ thick undoped P3AT samples, were in excess of 25 counts per second. In the best case, a $200\mu m$ multilayer stack of P3OT gave integrated count rates exceeding 2000 cps for the most intense scattering features.

The detector head consists of a vacuum dewar with a high purity beryllium entrance window (125μm thick). The detector element is a EG&G Reticon 1024S self-scanned silicon photodiode array with a heavy metal mask which shields all but the photosensitive array from exposure to the x-rays. The array actually consists of 1024 pixels with only ~960 pixels remaining unshielded. An analog signal is accumulated for each pixel over an exposure interval and is eventually converted via a 14-bit analog-to-digital converter (ADC). Software internal to the ADC allows the user to group pixels for output pixel widths of 25, 50, 100, 200, 400, and 800μm. The larger resolutions provide several times greater signal with only a single sampling of preamplifier noise for each detector read. Detector efficiency results in the single adsorption of a CuK_α photon yielding 0.8 detector counts after conversion.

Conceptually, the operation of the detector is simple. The photodiode array consists of a series of reverse-biased silicon diodes which effectively act as an array of capacitors. These capacitors cannot discharge because of the existence of a charge carrier free depletion region spanning each photodiode p-n junction. The absorption of an x-ray in this depletion region creates electron-hole pairs which discharge the capacitor in proportion to the number of electron-hole pairs created. At the end of an exposure time, the remaining charge on each photodiode is sent to a low-noise pre-amplifier.

The working temperature for the detector was originally designed in the 5° to -20°C temperature range with the photodiode array thermoelectrically regulated with a peltier. At these temperatures, the single scan integration time is limited by dark current and noise. In general, the temperature servo electronics and software normally limit the temperature to about -40°C. In order to reduce the dark current and thermal noise on the detector, some modifications have been made. First the thermal link between the thermoelectric element and the detector head case has been modified in a way that provides better thermal insulation. Secondly, chilled (-12°C) antifreeze solution was used as a detector coolant. These modifications allow detector cooling as low as -50°C. A vacuum system with a roughing pump and diffusion pump are used to support the detector. The use of vacuum in the detector prevents moisture condensation on the diode array and provides a good thermal insulation between the detector array and the detector case.

Each individual θ-2θ data run made by the detector, referred to as a "scan", is composed of a number of individual detector "steps". In order to minimize non-linearities across the detector, a correction factor for each pixel grouping is included and applied to each step, while the 2θ step size for each individual data collection point is limited to less than 0.5° (typically 0.3°). This 0.3-0.5° resolution results in each data point being an average integrated value based on 8-14 points spread evenly across the detector, in effect reducing non-linearities by averaging across the entire detector array.

For each diffraction scan, a background step is taken whereby data is collected with while no x-rays are present. This background step corrects for the average number of dark counts (thermal counts) per pixel. The background is subtracted from all subsequent scan steps. A dummy scan must also be implemented at the beginning of each data run because of observed background drift related to detector warm-up. It has also been noted that this particular detector has a repeatable pattern of background irregularities that vary as a function of individual step acquisition time, and pixel resolution. Both average background level and average variation from pixel-to-pixel repeat over some characteristic number of scans (typically 4-16). Although this is generally a small effect (average background varying by at most 20 counts), it can be a significant problem for resolving weak features (1-2cps). The cause of this irregularity has not been determined, but is most likely a result of some internal electrical noise. The 2θ overlapping for each data collection step has provided for some correction of this effect, consequently averaging out most of the problems associated with this erratic background. Of the 1024 pixels available on the detector, a small portion of these are masked by shielding defining the entrance window. These masked pixels are used to determine the average background level for each scan step improving the correction of this observed behavior.

For all diffraction scans, radial θ-2θ steps were performed with the sample mounted within the Eulerian cradle. By repositioning the sample both the equatorial and non-equatorial scattering could be acquired.

2.2.3 120° Detector and Diffractometer

This x-ray diffraction port is optimized for the acquisition of "powder" diffraction spectra from polymer films, but can also be used to acquire equatorial and non-equatorial scattering from partially oriented polymer films. The advantage of this setup is the ability for short acquisition times because of the 120° simultaneous data acquisition.

Diffractometer instrumentation consists of an elastically bent LiF monochrometer, an INEL CPS120 "wire" detector designed around a blade anode [51], allowing for a simultaneous 120° 2θ of data acquisition with a minimum pixel resolution width of 0.00732°, a pair of stepping motors to control sample orientation, and fully enclosed helium beam paths keeping air scatter to a minimum.

The detector performs essentially as a gas-ionization chamber using a curved blade rather than a wire as the anode. The sharp edge of the blade creates a zone of high electric field providing for high electron multiplication of x-ray photon ionized molecules. The cathode plane is a printed board consisting of copper strips which determine the centroid of the charge induced by the electron avalanche. A simple delay-line readout method provides information about the centroid location within the detector. A "self-quenching streamer" mode is used to prevent over ionization of the 15%/85% Ethane/Argon gas mixture. Because of the printed-board cathode and curved blade anode design, the detector has been found to have small errors in linearity on the order of a $\Delta_{2\theta}$ difference of 0.006° [52].

Long term detector background studies using a Fe^{57} source revealed systematic and reproducible pixel-to-pixel intensity variations of up to 0.5%. This non-linearity of response has been found to drift very slowly over long time periods. This effect has been periodically corrected for by taking detector backgrounds with the Fe^{57} source with sufficient statistics (48 hours to reduce pixel-to-pixel errors to 0.2%).

2.3 Sample Manipulation/Preparation

2.3.1 Regiospecificity

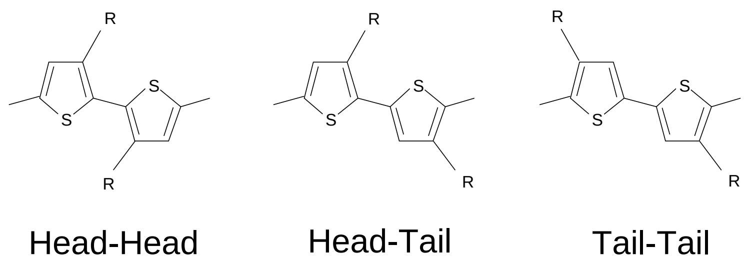

Figure 2.7: The chemical structure of P3ATs detailing the three possible types of side chain couplings to PT main chains.

It is important to note here one significant feature that distinguishes two different types of P3AT films examined in this thesis. Regiospecificity can be defined as the ability to determine exactly where a side chain will is attached to the conjugated polymer backbone. The side chain addition, when coupled with controlled synthesis, has been shown to dramatically enhance key electronic properties and profoundly alter the macromolecular structures [16,40,42,53]. P3ATs consist of an all *trans*-planar main chain which has a doubled monomer unit c-axis repeat of ~7.8Å. There are three possible monomer-to-monomer side chain couplings, head-to-tail (HT), head-to-head, and tail-to-tail as shown in Fig. 2.7. The ability to specify the extent of P3AT chemical regularity [16,54,15], with respect to side chain positioning, has been shown to significantly increase the maximum observable conductivities as well as focused attention on the role that side chains play. Both films with less regiospecificity (75% HT linkages) or regioirregular-P3AT films (IR-P3ATs) and films with almost complete regiospecificity (≥93% HT linkages) or regioregular-P3AT films (R-P3ATs) have been examined as part of this thesis.

2.3.2 IR-P3AT Films

Experiments in this thesis have mainly utilized polymer samples synthesized by Neste Oy (P3OT) and at Santa Barbara (P3HT and P3DDT) by direct oxidative coupling of the respective 3-alkylthiophene with $FeCl_3$ [53]. The molecular weights were typically M_w=80 000 and M_n=20 000. After synthesis, the $FeCl_3$ was extracted and the films dissolved in chloroform. These solutions were then filtered and immediately poured directly onto glass slides. After solvent evaporation, the films were lifted by methanol and clamped into a simple stretching device. Uniaxial stretching ratios of $\sim$4:1 were typically achieved at drawing temperatures ca. 100°C, producing film thicknesses of approximately 40μ [55,56]. These samples were then stored in a clamped state at room temperature until needed (anywhere from a month to a couple of years). Both casting and uniaxial stretching introduced anisotropy in spatial distribution of the crystallite fractions so that a full three-dimensional texturing was observed. NMR studies indicate that, on average, 25% of the alkyl chains are configured with head-to-head bonding arrangements [42].

For x-ray diffraction experiments, these cast and stretched films were cut, stacked, and mounted into a holding cell. For elevated temperature studies, samples were placed into a home-built furnace equipped with resistive cartridge heaters and a three-term PID temperature controller (Omega CN2010). For reduced temperature studies, the samples were mounted to the cold-finger of a closed cycle He cryostat equipped with a beryllium windowed vacuum shroud (see Fig. 2.8).

2.3.3 R-P3AT Films

The regioregular P3AT samples used in this thesis were synthesized at Carnegie Mellon by the polymerization of 2-bromo-5-(bromomagnesio)-2-alkylthiophene using catalytic amounts of Ni(dppp)Cl_2 [57]. The final polymer has essentially uniform regiochemical HT coupling when compared to polymers synthesized by direct oxidative coupling methods [53]. The molecular weights were typically M_w=42 000 and M_n=32 000 [15]. R-P3OT and R-P3DDT films were formed by evaporation in air of 1-3% (by weight) polymer/*m*-xylene solutions onto thin mica sheets at both room temperature and ca. 60°C. The samples cast at 60°C formed in 1-3 hours and resulted in a blackish, shiny, flexible "film" (type-I). The room temperature films were obtained by first heating the polymer/*m*-xylene mixture until the polymer completely dissolved and then cooling. These samples required from 1-2 days to form and gave a very different appearance. As the solvent evaporated a swollen gel-like phase first appeared and shrank. As the residual solvent left, the "films" broke apart into a large number of smaller flaky pieces (type-II) which were dark and brittle (see section 3.5 for a complete discussion of type-I and type-II structural types).

2.3.4 Cold Finger

For studying the temperature effects on the undoped polymer structure, a closed-cycle helium cryostat was used. It consists of a cold head, GB15, and a compressor, CP415. The cold head has two parts, the motor assembly and a cold finger assembly. The compressor supplies compressed helium to the cold head through stainless steel, flexible lines. The cold head achieves the Gifford-McMahon cycle by expanding the high pressure helium to low pressure. This is repeated 144 times per minute. The timing is controlled by a rotary valve

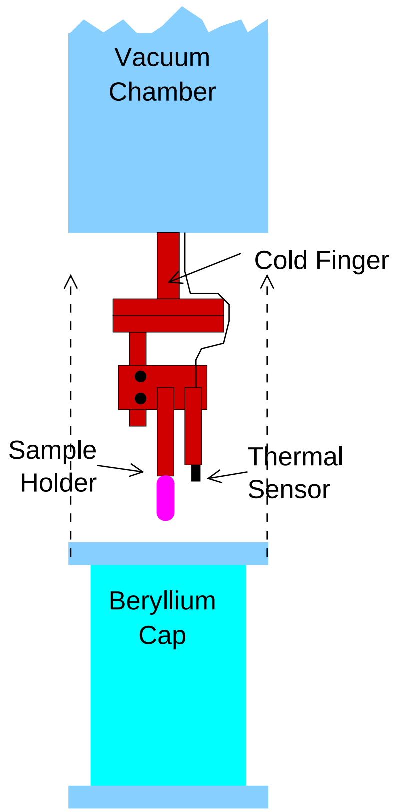

Figure 2.8: Schematic of the cold finger assembly used to study polymers at reduced temperatures.

which activates the displacers and the flow of helium through the regenerators, across heat exchangers and charging the expansion volumes with high pressure helium. The the rotary valve turns 45° and the high pressure helium is allowed to expand out of the expansion volume, across the heat exchanger and through the regenerator, back to the low pressure side of the compressor. The cold finger was mounted in a vacuum chamber with a beryllium cap at the bottom, which was a 3" high cylindrical tube with a 2.5" diameter and a 250μm thick wall, sealed to the aluminum base (see Fig. 2.8). The beryllium cap was able to withstand the 5x10^{-6} torr. This system, in principle, allows for the cooling of polymer samples down to 4.5°K.

2.3.5 Doping Cell

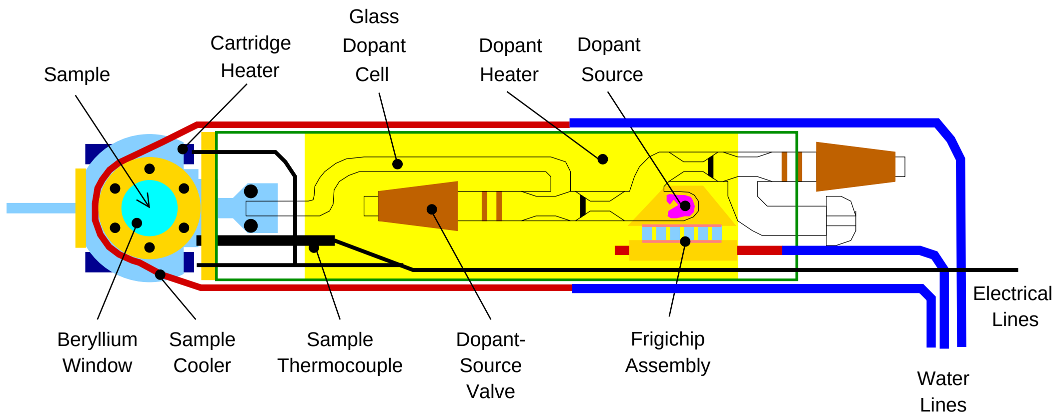

Figure 2.9: Vapor doping cell used for *in situ* x-ray diffraction polymer studies.

The stainless steel and glass *in situ* vapor doping cell contained separate sample and iodine source chambers that utilize separate temperature set points for the control of doping kinetics via changes in dopant vapor pressure.

The vapor dopant source was contained in the glass portion of the cell (see Fig. 2.9), with two valves isolating the dopant source from the sample chamber and the primary vacuum source. A water cooled Melcor Frigichip (CP1.0-31-05C) was able to cool a portion of the glassware to a minimum temperature of -10°C, while the entire glassware assembly was housed in an aluminum cylinder lined with a foil heater. Temperatures were monitored by an Omega CO3-J iron/constantan surface mount thermocouple sensor and stabilized with an Omega CN9000 temperature controller. This setup allowed for good control of the dopant temperature from -10°C to 180°C.

The sample chamber consisted of a stainless steel holder, two Omega cartridge heaters, two composite beryllium windows, a water cooled face plate, and a swagelock fitting that connected the glassware section to the stainless steel sample holder. Temperatures were monitored by an Hypodermic platinum resistor probe (Omega HYP-4) and stabilized with an Omega CN2011 temperature controller. This allowed for a controlled temperature range of 5°C to well over 200°C. The complete cell was entirely vacuum compatible.

Early versions of this cell were equipped with .0002"-.0003" mica windows allowing only for a partial vacuum within the cell. This partial vacuum inhibited control of the doping kinetics. A thin beryllium window allowed for complete evacuation of the cell, but iodine vapor was found to attack the untreated beryllium surface. A beryllium/epoxy/mica composite was developed to allow for a minimal amount of x-ray absorbtion, an evacuated system, and a chemically resistant cell. In the final version, the beryllium foils had a 2000Å layer of Nickel evaporated onto the inside surface of the windows. Total window absorption was limited to $\leq$2.5% each.

A single $5\mu m$ diameter nickel wire was also simultaneously mounted at the polymer surface. This enabled a straightforward determination of iodine concentration by periodically monitoring the intensity of the Ni (111) Bragg reflection. Alternatively, one could also monitor changes in both cell window Be and Ni (111) Bragg reflections, to calculate changes in sample absorbtion.

For doping level calculations, I_3^- is assumed to be the most prevalent iodine anion because of prior Mössbauer [58–60] and x-ray [61] studies of PA, and because of simple free volume considerations with the intercalant channels, although a recent study of aqueous iodine-doped P3OT has found that I_5^- is the major constituent in "fully" doped samples [62]. For simplicity, the iodine concentrations have been referenced throughout this paper to a presupposed, all I_3^- composition, but the presence of other polyiodide anion species cannot be ruled out.

By varying the relative temperatures at dopant source and sample zones, one controls how much dopant intercalates into the polymer sample by tuning the resulting vapor pressure and chemical potential. It will be shown that the experimenter can both push the dopant into the polymer host to very high levels, and pull most of the dopant back out with few complications.

2.4 Data Acquisition, Refinement, and Analysis

2.4.1 The Ewald Construction

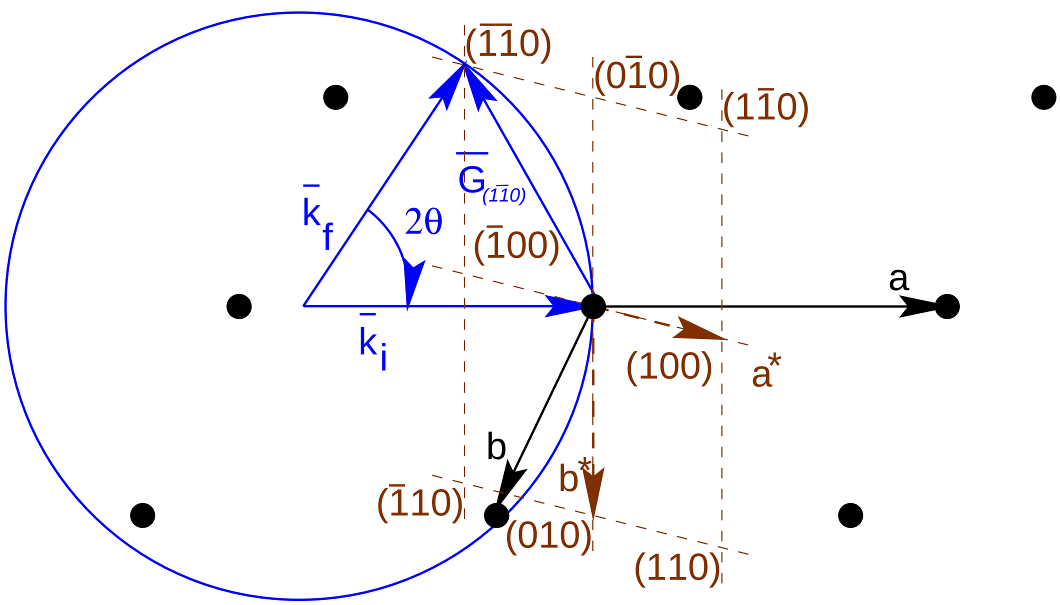

Figure 2.10: Ewald representation of scattering from 2-dimensional crystal lattice (black circles). The reciprocal lattice points are located at the intersection of the dashed lines. For incident radiation $\vec{k_i}$ one may observe the $(\bar{1}\bar{1}0)$ diffraction feature in the direction of $\vec{k_f}$

The reciprocal-lattice concept was originated by Ewald [63] and it is extremely useful for describing the origins of observed crystal diffraction patterns. A crystal can be defined in terms of a lattice of regularly spaced points in three dimensions. Each lattice point has associated with it a number of atoms at specific positions relative to that lattice point. This group of atoms is referred to as a "unit cell". Mathematically, one can describe the position of any individual lattice point by a translation of the unit cell

$$\vec{t_m} = m_1\vec{a} + m_2\vec{b} + m_3\vec{c} \tag{2.1}$$

by some integer combination of the three basis vectors $\vec{a}$, $\vec{b}$, and $\vec{c}$. Translating by combinations of all integers m_1, m_2, and m_3 would map out an infinite, perfect crystal. The set of vectors $\vec{G}$ that satisfy the equation

$$e^{i\vec{G}\cdot\vec{t_m}} = 1, \tag{2.2}$$

are known as the "reciprocal lattice" vectors, and combinations of these vectors map out all the possible Bragg reflections that result from the underlying crystal periodicities.

$$\vec{G_{hk\ell}} = h\vec{a}^* + k\vec{b}^* + \ell\vec{c}^* \tag{2.3}$$

The reciprocal lattice vectors can be written in terms of the original crystal lattice vectors:

$$\vec{a}^* = 2\pi\frac{\vec{b}\times\vec{c}}{\vec{a}\cdot(\vec{b}\times\vec{c})}\ ;\ \vec{b}^* = 2\pi\frac{\vec{c}\times\vec{a}}{\vec{a}\cdot(\vec{b}\times\vec{c})}\ ;\ \vec{c}^* = 2\pi\frac{\vec{a}\times\vec{b}}{\vec{a}\cdot(\vec{b}\times\vec{c})}. \tag{2.4}$$

The simple relationship between scattering angle θ, radiation wavelength λ, d-spacing between Bragg planes, and reciprocal lattice vector $\vec{G_{hk\ell}}$

$$\frac{n}{2d} = \frac{\sin\theta}{\lambda} = \frac{|\vec{G}_{hk\ell}|}{2} \tag{2.5}$$

makes the Ewald construction possible.

The method of Ewald, as illustrated in Fig. 2.10 for a 2-dimensional lattice, allows one to pictorially describe when and how various planes of atoms can be brought into the Bragg condition. First, one draws a vector of length $1/\lambda$ ($\vec{k_i}$) extinguishing at the origin of the reciprocal lattice. The direction of this vector is equivalent to the direction of the incident x-ray beam. Next, the origin of this vector becomes the center a sphere of radius $1/\lambda$. All reciprocal lattice points intersecting the surface of the sphere correspond to sets of Bragg planes that satisfy the condition for constructive interference. In Fig. 2.10, the only reciprocal lattice point that satisfies the Bragg condition for photons incident in the direction shown is the $(\overline{1}\overline{1}0)$ peak. The observed diffraction spot seen in the direction defined by the center of the sphere and the reciprocal lattice point ($\vec{k_f}$), or alternatively at an angle 2θ from the source determined from equation 2.5. So, if one were to put a single crystal, described by the pictured reciprocal lattice, in an x-ray beam of wavelength λ, with the orientation equivalent to $\vec{k_i}$, than one might observe diffraction features in directions coincident with $\vec{k_f}$ that intersect reciprocal lattice points on the Ewald sphere surface.

Powder diffraction refers to the scattering that originates from samples that are composed of a large number of randomly oriented crystallites. This has the effect of bringing all accessible planes into the Bragg condition for any incident x-ray direction. This is equivalent to taking the reciprocal lattice and rotating it about the origin in all directions. The reciprocal lattice becomes a series of concentric spheres that intersect the Ewald sphere at diffraction rings.

Stretch oriented polymers have a more anisotropic symmetry. Crystallites in these polymers have preferential orientation in one direction, but are random orientation in the plane perpendicular to the stretching direction. This has the effect of rotating the reciprocal lattice in a circle about the reciprocal lattice origin as shown in Fig. 2.11. The result is reciprocal circles that are located in equally spaced layers. Where the reciprocal circles intersect with the Ewald sphere one may observe a diffraction spots. This "layered" diffraction pattern

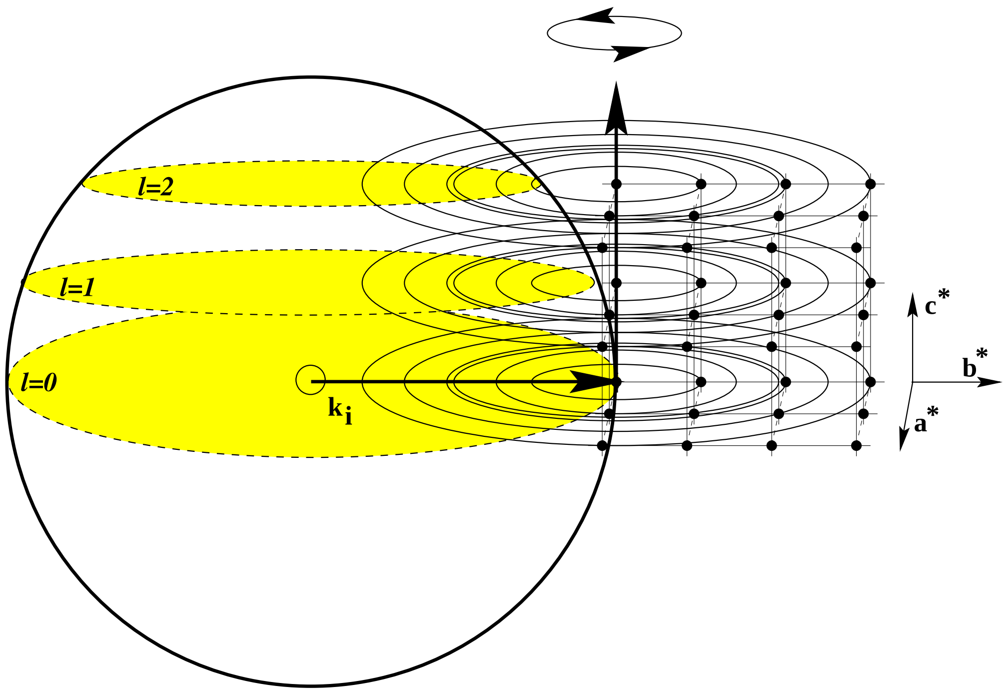

Figure 2.11: Ewald representation for systems possessing cylindrical symmetry. The observed diffraction from such a system consists of "layers" of diffraction arcs labeled here as ℓ=0,1,2. Diffraction from the ℓ=0 layer is commonly called equatorial scattering.

is what is observed for stretch oriented P3AT samples studied in this thesis.

2.4.2 Data Acquisition

For oriented polymer films, it is desirable to have complete scattering information about the crystallites that make up the polymer. The stretch-oriented P3AT polymer films studied here, to first order, can be considered as having cylindrically symmetrical distributions of crystallites giving the diffraction patter described in the previous section.

The orientation of a polymer film in an x-ray beam is defined by two angles

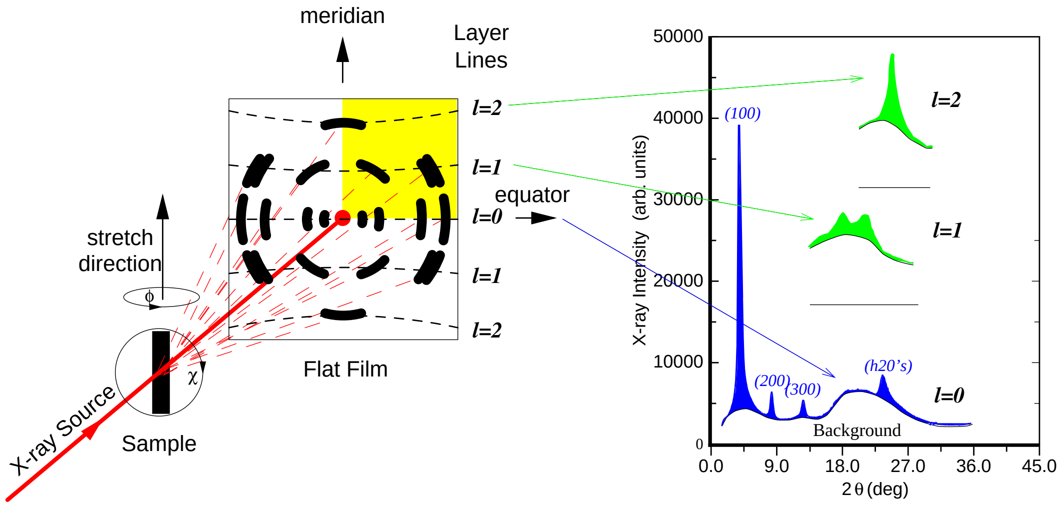

Figure 2.12: Diagram of the process involved in converting "flat-film" diffraction patterns into layer lines formatted suitably for structure factor refinement.

χ and ϕ, with χ describing the orientation of the polymer in the plane perpendicular to the incident beam and ϕ defining the angle between the film face and the incident beam about the stretch axis of the polymer (also referred to as the c-axis) as shown if Fig. 2.12. With transmission geometry defining the zero orientation of the polymer, the film is oriented so that the **c**-axis of the polymer is perpendicular to the detector plane, and the polymer face is perpendicular to the incident beam.

χ Map

For a polymer film oriented at fixed angles χ and ϕ, a θ-2θ scan provides scattering information only from Bragg planes oriented at an angle χ and making an angle of ϕ with respect to planes oriented perpendicular to the film face, and parallel to the **c**-axis. For a scattering angle 2θ, the polymer is necessarily rotated an angle θ in the detector plane. The sample was maintained in a symmetrical transmission geometry and the c-axis angle, with respect to the

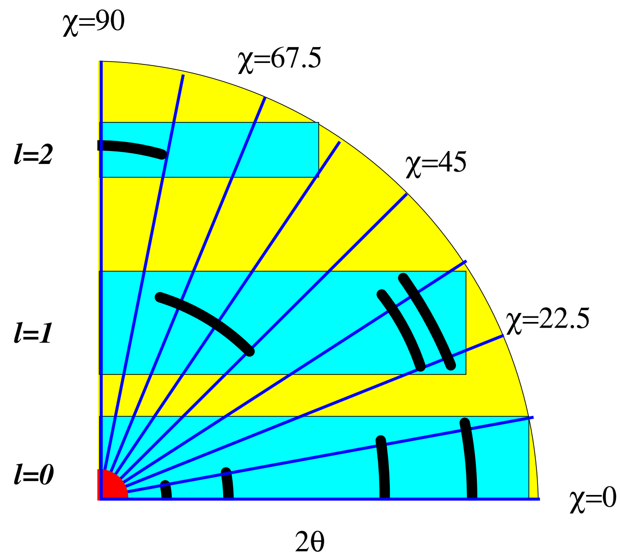

Figure 2.13: An equal intensity contour map, shown here, is composed of a number of θ-2θ scans at equally spaced intervals χ. Layer lines spectra used for structure factor refinement are converted from the shaded regions for each respective layer line.

scattering plane of the detector, set at 5°, 6°, or 10° increments from parallel to perpendicular. By acquiring data for various angles χ (see Fig. 2.13), one builds up an image that approximates 1/4 of the traditional flat-film photograph with two important distinctions. A flat-film photograph has distortions resulting from the flat plane in which the film resides, and has information about Bragg planes that depends on the angle of diffraction. This second distinction can be negated by simply not performing a θ-2θ scan and instead leaving the sample fixed while the detector moves to the scattering angle 2θ.

ϕ Map

By holding χ constant and taking θ-2θ scans as a function of ϕ one can investigate departures from the assumed cylindrical symmetry of crystallites within the polymer. The "ϕ Maps" shown in this work are solely those investigating equatorial anisotropy (χ=0) as shown in Fig. 2.14. To examine the anisotropy within the equatorial plane, sequential radial scans were executed with the samples rotated at 10° or 15° increments about the c-axis. The resulting data was then mapped into a single image by drawing constant intensity contours.

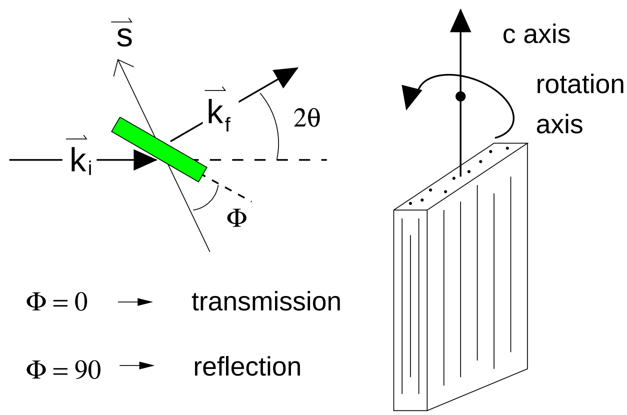

Figure 2.14: Schematic showing the geometry used for obtaining the equatorial anisotropy of P3AT cast-films. $\vec{k_i}$ is the incident beam and $\vec{k_f}$ is the scattered beam and $\vec{s}$ is the scattering vector.

2.4.3 Calculation of WAXS Diffraction Profiles

Calculation of wide-angle x-ray scattering profile intensities for comparison with polymer film and fiber diffraction data has a well-established methodology [64]. Due to the structural complexity intrinsic to these side chain substituted P3AT compounds, this study has been restricted to analysis of scattering features which arise from clearly represented periodicities in the polymer host. All other scattering features are treated collectively as constituents in various background profiles. Additionally, these models and subsequent structure factor calculations have not, as yet, incorporated intramolecular and intermolecular packing energies.

The method of computing x-ray structure factors closely follows the procedure outlined in Ref. [65]. For all P3ATs studied we assume that there is an appropriate 3-dimensional unit cell in which the chain axis of the polymer lies parallel to the c-axis. All intramolecular atomic positions are considered invariant except for the introduction of a minimal set of free parameters. These are discussed in greater detail in the next chapter. Individual lattice reflection intensities, $I_{calc}(hk\ell)$, were calculated using

$$I_{calc}(hk\ell) = P(\theta)L(\theta)|F(hk\ell)|^2 \tag{2.6}$$

where $F(hk\ell)$ is the structure factor, θ represents the Bragg angle, $P(\theta)$ is the polarization factor and

$$L(\theta) = 1/\sin^2\theta\cos\theta \tag{2.7}$$

is the Lorentz factor appropriate for powder samples. More complex forms of the Lorentz factor can be utilized for highly oriented polymer samples [65] but the large c-axis mosaics in these P3AT samples limited their usefulness. Correction factors for changes in scattering volume were not employed.

In the case $\ell = 0$ the samples were fully illuminated by the incident beam while for non-zero ℓ this factor is, given our specific treatment and limitations of the experimental data, not generally necessary. The explicit form of the structure factor is

$$F(hk\ell) = \sum_{j=1}^{N} f_j(sin\theta/\lambda)\exp(i\vec{G}_{hk\ell}\cdot\vec{r_j})M(\vec{G}_{hk\ell}) \tag{2.8}$$

in which there are N atoms within the unit cell, $\lambda = 1.542$Å, $\vec{G}_{hk\ell}$ is a reciprocal lattice vector, $\vec{r}_j$ is the position of the j_{th} atom, f_j is the atomic form factor [66], and $M(\vec{G}_{hk\ell})$ is an anisotropic Debye temperature factor. The actual values for Debye parameters are, at best, qualitative and are not explicitly stated in the text. In addition the actual number of requisite Fourier sums can be reduced by taking advantage of any translational symmetries between chemical subunits within the lattice basis.

An anisotropic Debye temperature factor has been implemented. Thermal vibrations of atoms cause a reduction in scattering as a function of diffraction angle θ and average vibrational amplitude spheroid described by $< \vec{\mu} >$.

$$M(\vec{G}_{hk\ell}) = e^{-16\pi^2|\vec{\mu}\cdot\vec{G}_{hk\ell}/2|^2} \tag{2.9}$$

As a result of the large unit cells employed, all structure factor calculations exhibited many closely spaced lattice reflections which were necessarily superimposed. Rather than perform a deconvolution of this data [67] or direct comparison with the entire experimentally obtained constant intensity contour maps [68], a customized hybrid procedure was implemented that achieved reasonable computational turnaround times so that a variety of structural models and subtle modifications could be rapidly investigated. In general, all non-zero intensity lattice reflections, $I_{calc}(hk\ell)$ were convoluted with a combined Lorentzian and Gaussian (pseudo-Voigt) function

$$C(2\theta)_{hk\ell} = \eta \exp\left[-4\ln 2\left(\frac{2\theta - 2\theta_{hk\ell}}{w}\right)^2\right] + (1-\eta)\frac{1}{1+4\left(\frac{2\theta-2\theta_{hk\ell}}{w}\right)^2} \tag{2.10}$$

where η is the relative Gaussian-Lorentzian weighting, w is the full width at half maximum of the peak and $\theta_{hk\ell}$ is the Bragg angle of a particular reflection.

The calculated radial profiles for each given ℓ layer line were obtained using

$$I_{calc}(2\theta) = \sum_{hk\ell} \sum_{2\theta_{min}}^{2\theta_{max}} I(hk\ell)C(2\theta)_{hk\ell}/d_{hk\ell} + B_{\ell}(2\theta) \tag{2.11}$$

where $B_{\ell}(2\theta)$ is an arbitrary and slowly varying background profile. The widths, d_{hkl}, of the isolated scattering features were adjusted independently (or by using a functionalized peak to peak coupling) while an average fixed width was assumed for all superimposed lattice reflections. This composite calculated scattering profile, combined with an appropriate background, could then be compared directly with scattering data from various layer lines which had been extracted from the constant x-ray intensity contour maps. Initially only the equatorial ($hk0$) scattering data were examined but then weighted (and appropriately scaled) $\ell = 1, 2, 3$ layer line profiles were incorporated into the fitting procedure. The relative deviation, R, was minimized according to the expression,

$$R = \frac{\sum_{\ell} \sum_{2\theta} (I_{calc} - I_{exp})^2 W(\ell, 2\theta)}{\sum_{\ell} \sum_{2\theta} (I_{exp})^2 W(\ell, 2\theta)} \tag{2.12}$$

where W is a relative weighting factor. It is important to note that the $\ell \neq 0$ scattering profiles are presented with respect to the actual Bragg angle 2θ and not in terms of their component equatorial wavevector parallel to the (hk0) plane.

2.4.4 Basic Model

The monomer used to construct all P3AT models for use in structure factor calculations is shown in Fig. 2.15. The bond lengths and angles for the main thiophene unit were obtained from x-ray diffraction [69,70] and intramolecular energy calculation of PT and constituent oligomers [71]. Standard tetrahedron angles of 109.47° and bond lengths of 1.53Å and 1.09Å were used for positioning carbon and hydrogen atoms respectively in constructing the all *trans* hexl, octyl, and dodecyl alkyl side chains.

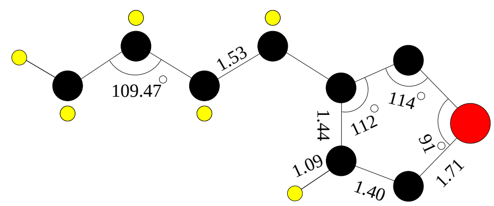

Figure 2.15: Basic structure of the base P3OT monomer used to construct unit cells as part of structure factor refinement. Non-degree numbers are in Å units.

The general features of the scattering data support a planar conformation of the thiophene rings and infrared absorption studies [40] suggest a large proportion of trans-planar bonding configurations for the alkyl side chains at room temperature. If these basic characteristics are rigidly enforced, then the only remaining allowed structural degrees of freedom are in the lattice parameters, rotation about the polymer chain axis (i.e. a setting angle, ϕ_R), rotation of the alkyl side chain about the C-C bond which connects to the thiophene backbone (a dihedral angle, θ_D), and, finally, changes in this C-C bond angle with respect to the chain axis direction, θ_B. These parameters are shown schematically in Fig. 2.16. In reality the actual physical situation is expected to be considerably more complicated and hence only the average direction of the alkyl side chain orientation is of meaningful significance.

The basic orthorhombic (or monoclinic) unit cells occasionally invoke arbitrary expansion of the unit cell in the attempt to incorporate a repeated disorder which is intended to mimic more general structural disorder. Most of the numbers reported in this thesis originate from a unit cell with an arbitrary doubling

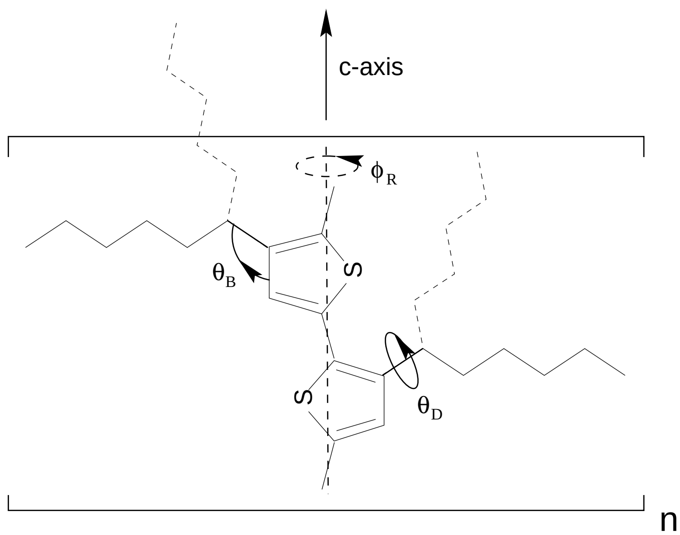

Figure 2.16: Degrees of freedom used in modeling calculations. The monomer shown here is P3HT.

of the interlayer spacing in order to esthetically include the two rotationally equivalent layer structures.

Additional parameters were necessary to account for iodine contributions to the scattering profiles. These factors included positional and orientational degrees of freedom in combination with a fractional site occupancy. Various species of molecular iodine were also tested. These included I_3^- and I_5^-, but the best fits were realized using an I_3^- trimer with interatomic spacings of close to 3.0Å [72,73]. At higher iodine compositions there was little difference between models with I_3^- or I_5^- species.

2.4.5 Corrections for Instrumental Broadening

For line profile analysis studies, data could be corrected for instrumental broadening by the method of iterative unfolding [74]. For data taken on the 120°

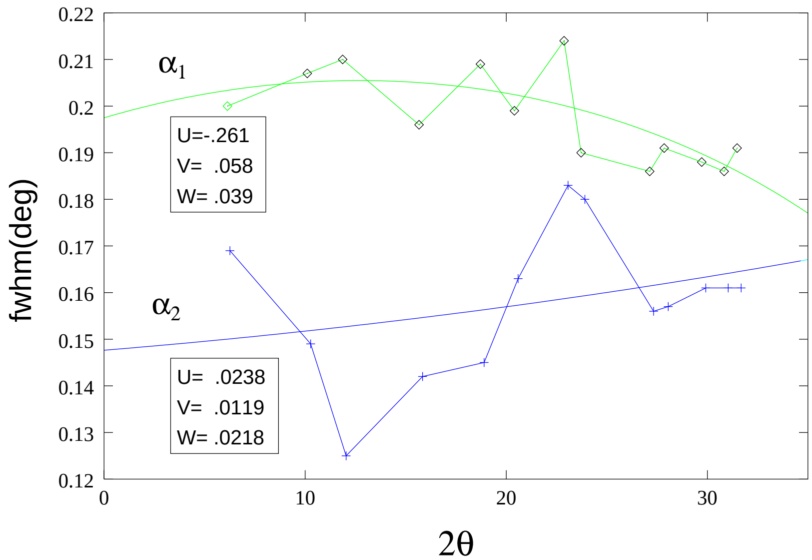

Figure 2.17: Plot of zeolite peak width as a function of angle. Peaks widths due to the α_1/α_2 character of the CuK_α x-ray beam have been plotted separately and fit to a pseudo-Voigt function $\mathrm{FWHM}^2 = U\tan^2\theta + V\tan\theta + W$.

detector port, a Y-52 zeolite powder sample was used as an instrumental standard. Resulting scattering profiles exhibited 13 strong, non-overlapping peaks in the range 6.0°-32.0° degrees 2θ. Because P3ATs all have their most statistically significant peak between $\sim 3.3°$ and $5.0°$ 2θ, and because there is not a peak from the instrumental standard at these angles, an approximated standard peak was used for this deconvolution. By fitting each zeolite reflection with two pseudo-Voigt shaped peaks, $\eta G + (1-\eta)L$ (where G and L are Gaussian and Lorentzian peaks with the same FWHM), to reproduce the partially superimposed K_{α_1,α_2} character for each instrumental peak. The measured peak widths were then fit [75] to $\mathrm{FWHM}^2 = U\tan^2\theta + V\tan\theta + W$. The measured values of η_{α_1} =0.60, $\eta_{\alpha_2} = 0.74$, and α_1/α_2 intensity ratio, at 3.33, remained relatively constant over the region of interest while the other values used for deconvolution of instrument from spectra follow: U_{α_1} = -.261, V_{α_1} = .0577, W_{α_1} = .0388, U_{α_2}

= .0238, V_{α_2} = .0119, and W_{α_2} = .0218.

2.4.6 Hardware/Software

Most of the computation preformed as part of this work was done on a VMS/VAX station 4000-60, although later computation was preformed on a VMS/Alpha station 200-4-166 which represented an order of magnitude increase in computational performance. Structure factor software necessitated frequent input from the user, consequently graphical interfaces were built into the software allowing the user to adjust model unit cells and see the resulting model spectra compared to each individual layer line. Because of the small number of observable diffraction peaks present in polymer systems, it is not possible to perform a conventional Rietveld type determination of crystal structure [76,77]. The small number of broad peaks precludes the elimination of various symmetries, so user input is necessary to obtain a model that approximates the observed diffraction spectra. Once an appropriate fit for a suggested model had been made, minimization algorithms could be used to find the "best-fit" parameters for the chosen structure.

For the 4-circle diffractometer port, computer software was written and designed to allow for automated data acquisition. Complete control of sample temperature was part of the data acquisition protocol, providing a useful degree of freedom for long term temperature studies.

Major software packages utilized for the above software and for necessary publishable documents include PGPLOT, XFIG, LATEX, and MINUIT.